IEEE Access
Multidisciplinary | Rapid Review | Open Access Journal

Received 17 August 2022, accepted 12 September 2022, date of publication 15 September 2022,
date of current version 23 September 2022.

Digital Object Identifier 10.1109/ACCESS.2022.3206774

RESEARCH ARTICLE

Novel Quasi-Three-Dimensional Modeling of Axial Flux In-Wheel Motor With Permanent Magnet Skew

KI-HOON KIM AND DONG-KYUN WOO
Department of Electrical Engineering, Yeungnam University, Gyeongsan, Gyeongbuk 38541, South Korea
Corresponding author: Dong-Kyun Woo (wdkyun@yu.ac.kr)

ABSTRACT This paper presents a characteristic analysis of axial flux permanent magnet machines (AFPMMs) for in-wheel electric vehicles. Preferentially, a novel quasi-3-D model is developed for the fast and accurate design of AFPMMs. In electromagnetic field analysis, combined with field reconstruction method, the computation time of 2-D solutions is significantly reduced. With the use of time sweeping of the basis function, only the static finite element (FE) analysis is performed to calculate the air-gap flux distribution at the entire rotor position, whereas the conventional 2-D solutions require a transient FE analysis. In the shape sweeping process of the basis function, the virtual air-gap section method is introduced to take into account that the ratio of slot opening to slot pitch is different depending on the radius of analysis plane, which causes errors in the analysis results of the conventional quasi-3-D method. The virtual air-gap sections are obtained by interpolation of the spatial field between the mapped cylindrical planes. The proposed technique reduces the number of 2-D analysis planes required for high accuracy in the conventional quasi-3-D method, and it can also predict the air-gap magnetic flux distribution for skewed permanent magnets without additional FE analysis. Finally, using the magnetic fields calculated in the proposed method, the electromagnetic performances of the AFPMM are calculated, such as load torque, cogging torque, attraction force, and back-EMF. The proposed method was used for the design of the AFPMM for a 5 kW in-wheel motor. The validity of analytical results is confirmed by 3-D FE and experimental results.

INDEX TERMS Axial flux permanent magnet machine, in-wheel motor, magnetic field reconstruction, permanent magnet skew, quasi-3-D finite element analysis, virtual air-gap section method.

I. INTRODUCTION

An axial flux permanent magnet machine (AFPMM) has become popular in the last few decades because it has a higher torque density at low speed in comparison with a radial flux permanent magnet machine [1], [2], [3], [4]. In particular, its structural features make it suitable as an in-wheel motor in electric vehicles [5], [6], [7], [8]. Since precise control in electric vehicles directly contributes to driving performance, accurate and rigorous design is required for driver comfort [9], [10], [11], [12].

The associate editor coordinating the review of this manuscript and approving it for publication was Ladislau Matekovits.

Due to the inherent structural characteristics of the AFPMM with radial non-uniformity, a three-dimensional (3-D) finite element (FE) analysis is required for accurate analysis and design. However, despite advances in software for the FE analysis and improvements in computational speed, the use of the 3-D FE analysis is still a significant computational burden on designers. Therefore, a quasi-3-D FE method has been developed to analyze the electromagnetic properties of the AFPMM, which slices the 3-D geometry into individual cylindrical planes [13], [14], [15], [16], [17], [18], [19]. It derives analysis results from 2-D solutions. Since this method relieves significant computational burden compared to the 3-D FE

analysis, it is efficient of iteration in the optimization design process. However, a sufficient number of 2-D analysis planes are required to achieve high accuracy matching the results of 3-D FE analysis. In applications with different design parameters, the sufficient number of 2-D solutions will be different to meet the required accuracy. In addition, it is difficult to consider the deformed shape of the stator and rotor used for performance improvement, such as permanent magnet skew.

In electromagnetic field analysis, the field reconstruction (FR) method has the advantage of reducing time cost [20], [21], [22], [23]. The FR method reconstructs the armature reaction field and the open-circuit field using a basis function. Each magnetic field is calculated by sweeping a magnetic field snapshot obtained by performing the static FE analysis. The total magnetic field corresponding to a specific position of the rotor or any excitation current can be obtained with simple mathematical calculations without additional FE analysis. Previous papers focusing on magnetic field analysis using the FR method in the AFPMM [21], [22] use the static FE analysis to obtain the magnetic field snapshots, which significantly reduces the computational cost compared to the conventional transient FE analysis with many analysis steps. However, the structural characteristics of AFPMM still require expensive 3-D static FE analysis, so its use in the optimization process can be burdensome.

The proposed technique with the new strategy is an improved quasi-3-D modeling based on the FR method. In electromagnetic field analysis of the proposed method, there are two types of sweeping magnetic flux distribution by the basis function, viz., time sweeping and shape sweeping. The time sweeping of the basis function predicts the magnetic flux distribution by the specific rotor position. In the conventional quasi-3-D technique, transient FE analysis for a long time is performed and a large number of analysis steps are required to ensure the accuracy of the analysis result. On the other hand, using the time sweeping, the armature reaction field is reconstructed to perform the static FE analysis with only 1 analysis step.

The shape sweeping of the basis function contributes to improving the accuracy of the quasi-3-D analysis. In the conventional quasi-3-D FE analysis in Fig. 1, the cylindrical plane is represented as the 2-D analysis plane and sliced into 4 pieces. Analysis models in each 2-D analysis plane have the same stack length of (*Ro-Ri*)/4. In the stator of the AFPMM, the ratio of slot opening to slot pitch decreases linearly along the radius of 2-D analysis plane, since slot openings are constant at different radii [24]. However, the 2-D analysis model does not take into account the ratio of the slot opening to the slot pitch and the air-gap length, which varies linearly with the radius. Therefore, enough 2-D analysis planes are needed for high accuracy. The introduced virtual air-gap section method provides a reduction in error by adjusting the magnetic flux distribution between a limited number of 2-D analysis planes. First, based on the Kriging method [25], [26], [27], [28], [29], the basis function interpolates the spatial field between neighboring 2-D analysis

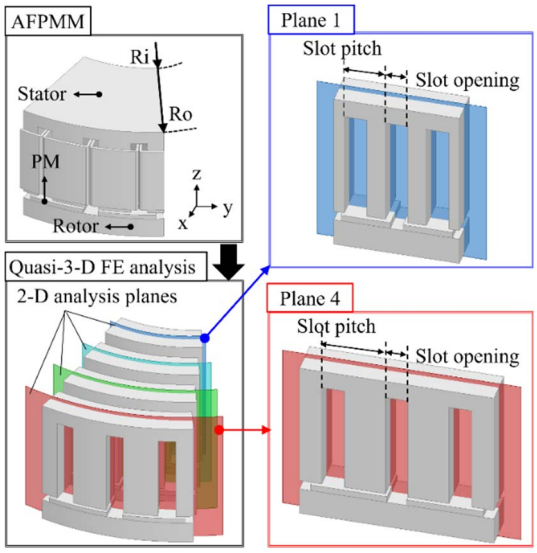

FIGURE 1. Qausi-3-D model of AFPMM.

planes. Then, the magnetic flux distributions on the virtual air-gap section are reconstructed. The reconstructed magnetic field is used to calculate the electromagnetic performances such as load torque, cogging torque, attraction force, and back-EMF.

In the previous research, numerous methods have been proposed for the reduction of cogging torque, such as fractional slot overlapping windings [30], [31], a new permanent magnet shape [32], [33], [34], auxiliary slot [35], [36], rotating tapering [37], and PM skew [38], [39], [40], [41]. Although many techniques for reducing cogging torque have been developed to contribute to the improvement of control quality, the trade-off between manufacturing cost and effectiveness remains a necessary task. Among those techniques, the permanent magnet (PM) skew has been widely used because deforming the shape of the stator is difficult to manufacture and ultimately increases the manufacturing cost. In particular, it should be taken into account that in-wheel motors are limited in axial length due to the spatial requirements in electric vehicles. Fortunately, combined with the fact that PMs in AFPMMs are flat, the PM skew reduces the cost and effort in fabrication [33], [42], [43], [44], [45]. However, when using the PM skew technique to reduce the cogging torque, it should be taken into account that other characteristics vary according to the changed skew angle [46]. Hence, the determination of the optimal PM skew angle is the result of a compromise between the characteristics in the optimization process. In the conventional quasi-3-D analysis, in order to select the optimal skew angle, the FE analysis of the AFPMM with the skew angle is inevitable whenever the skew angle is changed. In the proposed method, the magnetic field according to the skew angle can be predicted without additional FE analysis by using the field reconstruction of the basis function. Compared with the conventional quasi-3-D FE analysis, the proposed method provides faster design optimization with high accuracy.

The rest of this paper is organized as follows. In section II, the armature reaction field interpretation of the AFPMM is presented, along with the introduction of the time sweeping and shape sweeping of the basis function. In section III, the open-circuit field reconstruction of the basis function and the calculation of the magnetic flux distribution for the PM skew are presented. In section IV, the characteristic analysis of the AFPMM using the reconstructed magnetic flux distribution is presented. In Section V, the results of the proposed method are verified by comparison with 3-D FE analysis results and experiments. Finally, in Section VI, the conclusion of this paper is presented.

II. QUASI-3-D MODEL OF ARMATURE REACTION FIELD

A. MAGNETIC FIELD RECONSTRUCTION USING TIME SWEEPING

The armature reaction field, the sum of the magnetic fields generated from the excitation current of the individual slot coils, is expressed as:

$$B_A(t, r, \theta) = \sum_{k=1}^{N_S} B_{A,k}(t, r, \theta) \tag{1}$$

where B_A is the total armature reaction field, $B_{A,k}$ is the magnetic field by the winding excitation current of the kth slot, and N_s is the number of slots. The field corresponding to each slot is calculated by the basis function of the armature reaction field as follows:

$$B_{A,k}(t, r, \theta) = f_A\left(t, r, \theta, B_{k,ref.}\right) \cdot i(t, \theta_k) \tag{2}$$

where f_A is the basis function of the armature reaction field, $B_{k,ref.}$ is the reference magnetic flux distribution in the air-gap with respect to the kth slot, and $i(t, \theta_k)$ is the excitation current with the current angle θ_k in the kth slot.

$B_{k,ref.}$ consists of air-gap flux distributions in each 2-D analysis plane, and these are obtained by performing static FE analysis with 1 analysis step with PMs excluded. In the static FE analysis, the initial DC current is excited in the slot winding as follows:

$$B_{k,ref.} = \left[B^1_{k,ref.}(\theta)\ B^2_{k,ref.}(\theta) \cdots B^N_{k,ref.}(\theta) \right] \tag{3}$$

$$B^N_{k,ref.}(\theta) = \left. \frac{B^N_{A,k}(\theta, I_0)}{I_0} \right|_{t=t_0} \tag{4}$$

where $B^N_{k.ref.}$ is the reference magnetic flux distribution in the Nth 2-D analysis plane, t_0 is the initial time, and I_0 is the initial DC current. It is noted that $B^N_{k.ref.}$ contains the shape information of the stator because the air-gap magnetic flux distribution obtained by the static FE analysis is divided by the applied current I_0.

Fig. 2 shows the reference magnetic flux distribution of the AFPMM. The AFPMM has 20 poles and 30 slots, with inner and outer diameters of 150mm and 285mm respectively. The 2-D analysis plane is located at a diameter of 108 mm. Fig. 2 (a) represents the FE analysis model for the armature reaction field. In slot winding, the initial current is excited and PM is excluded. Using (4), Fig. 2 (b) and (c) show the z-component and θ-component of the reference magnetic flux distribution on the air-gap of 36 degrees corresponding to one period, respectively.

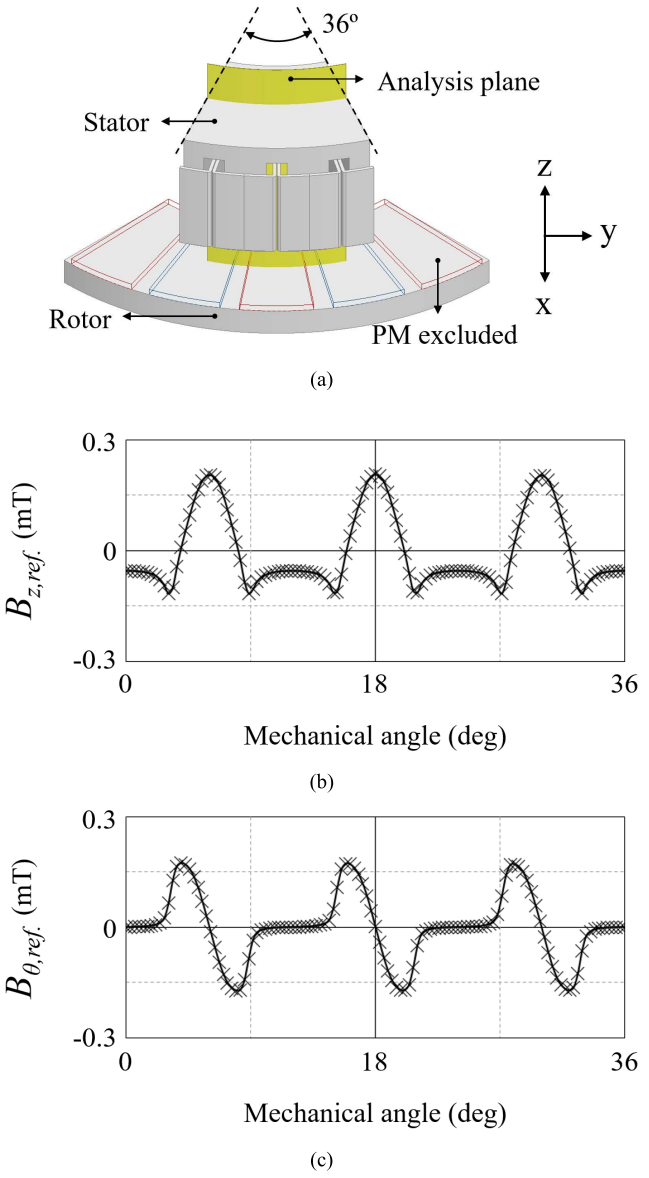

FIGURE 2. (a) 2-D analysis plane with a radius of 108 mm. (b) The z-direction component of the reference magnetic flux distribution. (c) The θ-direction component of the reference magnetic flux distribution.

Using the reference magnetic flux distribution, the basis function performs the time sweeping over the entire time period in (2). In the time sweeping, only simple mathematical calculations are required to obtain the transient result. The basis function also makes it possible to predict the armature reaction field for specific excitation current without additional FE analysis. Therefore, it can provide significant time cost reduction compared to the conventional transient FE analysis. In Fig. 3, the reconstructed armature reaction field at a specific rotor position is shown. It was calculated in (2) using the reference magnetic flux distribution in Fig. 2. The

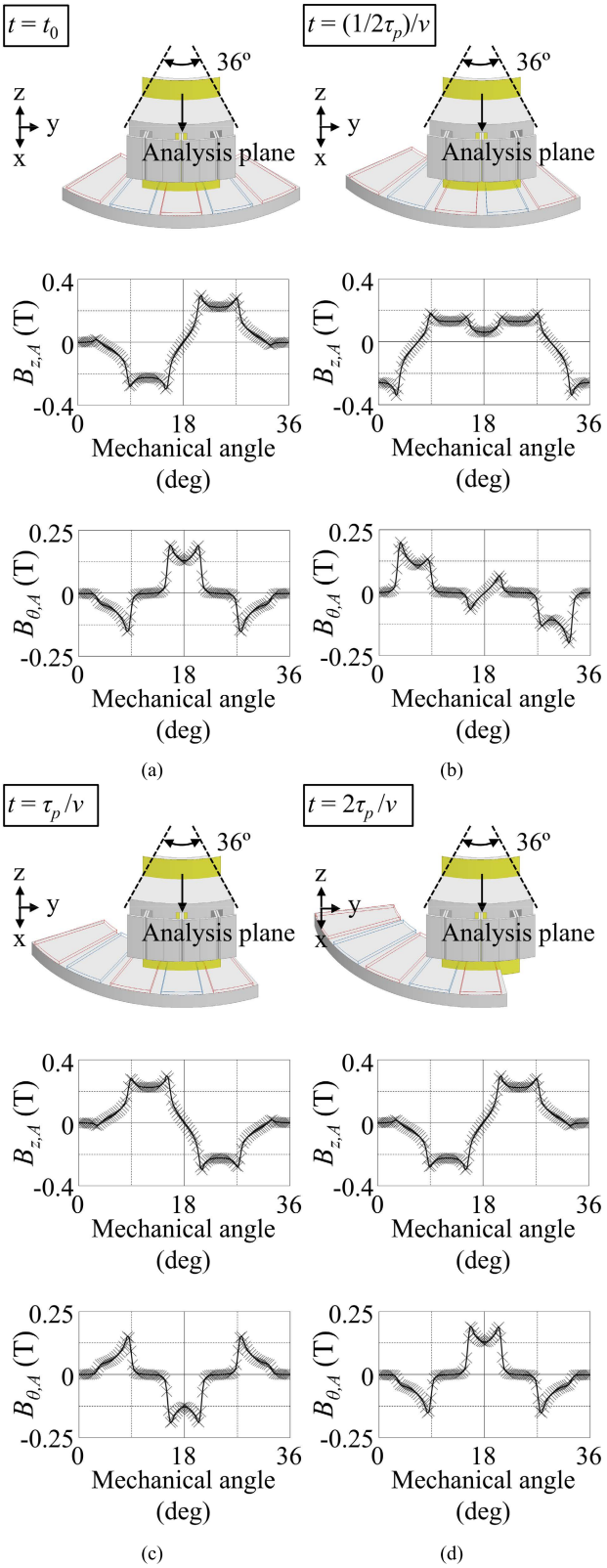

FIGURE 3. Armature reaction field. (a) Initial time. (b) Rotor moves by 1/2 pole pitch. (c) Rotor moves by pole pitch. (d) Rotor moves by 2 pole pitch.

rotor is located at the initial position, $1/2\tau_p$, τ_p, and $2\tau_p$, respectively, and τ_p is the pole pitch. t_0 is the initial time

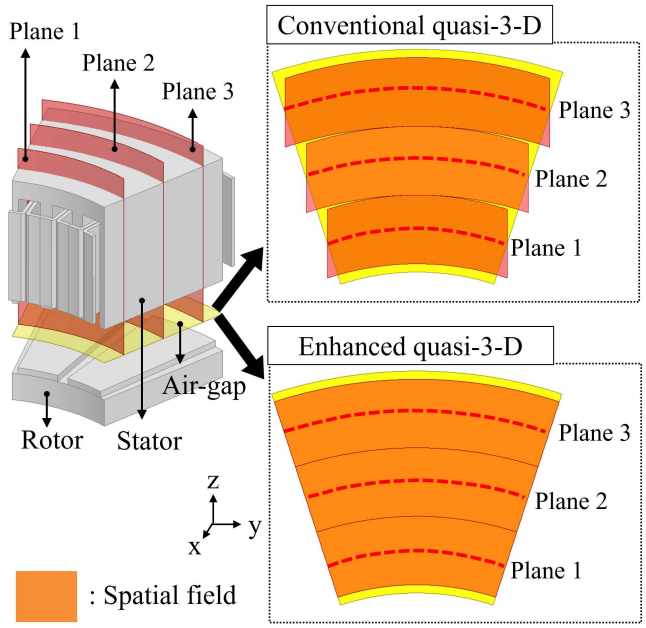

FIGURE 4. 2-D analysis plane in the air-gap of AFPMM.

and v is the motor speed of the AFPMM. $B_{z,A}$ and $B_{\theta,A}$ are the z-direction and θ-direction components of the armature reaction field, respectively. The slot winding is excited with a current of 28A and the respective current angles are 0, $2\pi/3$ and $-2\pi/3$. It can be seen that the armature reaction field has a period of 2 pole pitches.

B. SHAPE SWEEPING USING KRIGING METHOD

Fig. 4 shows the air-gap region and 2-D analysis planes in the conventional quasi-3-D analysis and in the enhanced one. In the conventional quasi-3-D method, it is assumed that the electromagnetic properties between neighboring 2-D analysis planes are the same. The spatial field between the 2-D analysis planes, however, has an enlarged shape along the radial direction. Therefore, the length of the air-gaps along the radius is different. Also, because of the parallel slot openings, the ratio of slot opening to slot pitch is not constant, which results in different electromagnetic properties in the air-gaps in the spatial field. For these reasons, a sufficient number of 2-D analysis models are needed to reduce the error with the analysis results of the 3-D FE method. The enhanced quasi-3-D shown in Fig. 4 is the method proposed in this paper, and the magnetic flux distribution on virtual air-gap sections between 2-D analysis planes are obtained through spatial interpolation.

Based on the Kriging method, the shape sweep of the basis function reconstructs the air-gap magnetic flux distribution. The Kriging method has been used in the optimization of electromagnetic machines as a spatial interpolation method that began to be used in the field of mining geology [25], [26], [27], [28], [29]. This technique predicts values of continuous spatial fields with high accuracy using limited sample data in the problem domain. First, the magnetic flux

TABLE 1. 2-D analysis plane.

Ri (mm)	75
Ro (mm)	142.5
Number of 2-D analysis plane	5
Number of virtual air-gap section	40
Radius of Plane 1 (mm)	75
Radius of Plane 2 (mm)	91.875
Radius of Plane 3 (mm)	108.75
Radius of Plane 4 (mm)	125.625
Radius of Plane 5 (mm)	142.5

distribution calculated in the 2-D analysis plane as sample data is mapped to the problem domain by a basis function. In Fig. 4, the problem domain is the air-gap region of the AFPMM, and the sample data is the reference magnetic flux distribution. Then, spatial interpolation with n lattices is performed to extract the magnetic flux distribution on the virtual air-gap section as

$$B_{A,k}^{N,\gamma}(t,\theta) = B_{A,k}\left(t, r_{N,\gamma}, \theta\right) \tag{5}$$

$$r_{N,\gamma} = \frac{(Ri+Ro)(N\cdot n+\gamma)}{P\cdot n} \tag{6}$$

where $B_{A,k}^{N,\gamma}$ is the armature reaction field for the γth virtual air-gap section in the interpolated spatial field corresponding to the Nth 2-D analysis plane, $r_{N,\gamma}$ is the radius of $B_{A,k}^{N,\gamma}$, P is the number of 2-D analysis planes, and n is the number of lattices in the Kriging method.

Fig. 5 shows the armature reaction field at the initial time ($t = t_0$). Fig. 5 (a) describes the analysis model of the AFPMM in the initial position and the range of the problem domain. The analysis model is the AFPMM with inner and outer radii of 75 and 142.5 mm, and the number of 2-D analysis planes is 5. The radius of each 2-D analysis plane is given in Table 1. In Fig. 5 (b) and (d), the z-component and θ-component of the armature reaction field in the 2-D analysis plane are shown, respectively. The 2-D solutions in each 2-D analysis plane are mapped to the problem domain and used for spatial interpolation using the Kriging method. In the interpolation process of the spatial field, the number of lattices is 10, and the z- and θ-components of the interpolated magnetic fields are shown in Fig. 5 (c) and (e). The basis function extracts the magnetic flux distribution in 10 virtual air-gaps between neighboring 2-D analysis planes. Since spatial interpolation is performed inside the sample data, there are 5 2-D analysis solutions and 40 virtual air-gap fields in the problem domain in Fig. 5, and a total of 45 magnetic flux distributions were obtained.

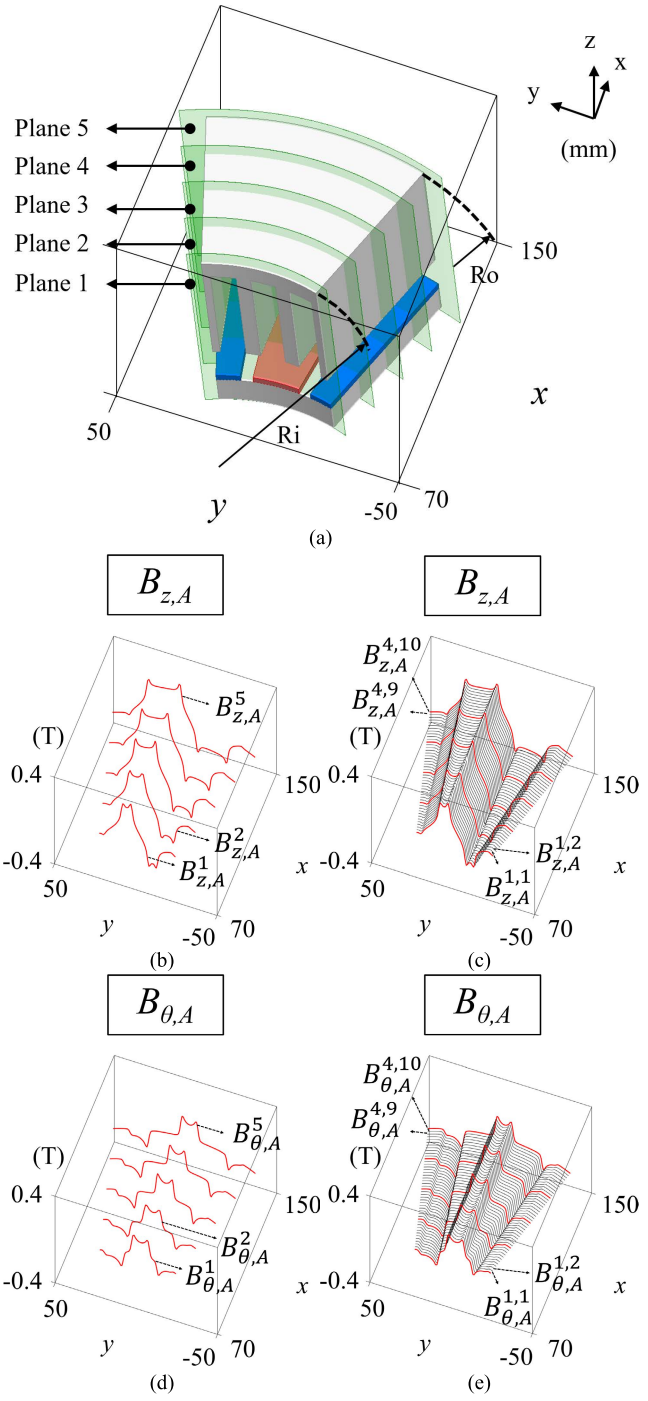

FIGURE 5. (a) 2-D analysis plane. (b) z-component of magnetic flux distribution of armature reaction field on 2-D analysis plane. (c) θ-component of magnetic flux distribution of armature reaction field on 2-D analysis plane. (d) z-component of reconstructed magnetic flux distribution in virtual air-gap section. (e) θ-component of reconstructed magnetic flux distribution in virtual air-gap section.

III. QUASI-3-D MODEL OF OPEN-CIRCUIT FIELD

A. OPEN-CIRCUIT FIELD RECONSTRUCTION

The open-circuit field is expressed as the sum of the magnetic fields generated by individual PMs as follows.

$$B_O(t,r,\theta) = \sum_{p=1}^{N_p} B_{O,p}(t,r,\theta) \tag{7}$$

where B_O is the total open-circuit field, $B_{O,p}$ is the field by the pth PM, and N_p is the number of PMs. Using the basis function of the open-circuit field, $B_{O,p}$ is reconstructed as

$$B_{O,p}(t,r,\theta) = f_O\left(t,r,\theta,B_{p,ref.}\right) \tag{8}$$

$$B_{p,ref.} = \left[B_{p,ref.}^1(\theta)\ B_{p,ref.}^2(\theta)\ \cdots\ B_{p,ref.}^N(\theta)\right] \tag{9}$$

where f_O is the basis function of the open-circuit field, and $B_{p,ref.}$ is the reference magnetic flux distribution. $B_{p,ref.}$ is obtained using FE analysis performed without excitation current under no-load condition. Since the open-circuit field repeats its shape at every two pole pitches, time sweeping of the basis function is performed as follows:

$$B_{O,p}\left(t + v/(2\tau_p), r, \theta - 2\tau_p\right) = B_{O,p}\left(t, r, \theta\right) \quad (10)$$

where v is the motor speed, and τ_p is the pole pitch.

Fig. 6 shows the air-gap magnetic flux distribution of the open-circuit field on the 2-D analysis plane corresponding to a radius of 108 mm. The open-circuit field in Fig. 6 is the distribution when the rotor is positioned at the initial position, 1/2 τ_p, τ_p, and 2 τ_p, respectively. $B_{z,O}$ and $B_{\theta,O}$ are the z-direction and θ-direction components of the open-circuit field, respectively. In Fig. 6, it can be seen that the open-circuit field repeats the waveform every 2 pole pitches.

B. PM SKEW

As one of many techniques for reducing cogging torque, the PM skew is well known for its high cost-effectiveness. In particular, in the AFPMM for in-wheel motor, it is difficult to apply techniques that require shape modification or end winding in the stator due to space and structural constraints. However, since the PM of AFPMM is flat, it is easier to shape the PM than RFPMM. The PM skew provides a reduction in the cogging torque, but at the same time affects other characteristics as well. Therefore, the optimal PM skew angle is determined as a result of a compromise of several electromagnetic properties. In the PM skew angle optimization process, the conventional quasi-3-D method requires iterative work of the FE analysis because different models are considered whenever the skew angle is changed. In the proposed technique, however, shape sweeping of the basis function makes it possible to predict the characteristic change according to the skew angle without additional FE analysis.

Fig. 7 shows the non-skewed and skewed PMs in the rotor of the AFPMM, where α_{skew} is the skew angle. In the same 2-D analysis plane, it can be seen that the rotor is shifted in the skew direction in the analysis model with skewed PM. Using the basis function of the open-circuit field, the air-gap magnetic flux distribution for the entire rotor position is reconstructed from (7)-(10). Therefore, the shifted magnetic flux distribution due to PM skew can be predicted. The air-gap magnetic flux distribution with PM skew applied is calculated as follows.

$$B_{O,p}^{N,\gamma}\left(t, \theta\right) = B_{O,p}\left(t, r_{N,\gamma}, \theta\right) \quad (11)$$

$$B_{O,p,skew}^{N,\gamma}\left(t\right) = B_{O,p}^{N,\gamma}\left(t + \frac{2\pi\left(r_{N,\gamma} - R_i\right)\alpha_{skew}}{360 \cdot v}\right) \quad (12)$$

where $B_{O,p}^{N,\gamma}$ is the open-circuit field for the γth virtual air-gap section in the interpolated spatial field corresponding to the Nth 2-D analysis plane. $B_{O,p,skew}^{N,\gamma}$ is the open-circuit fields with the PM skew.

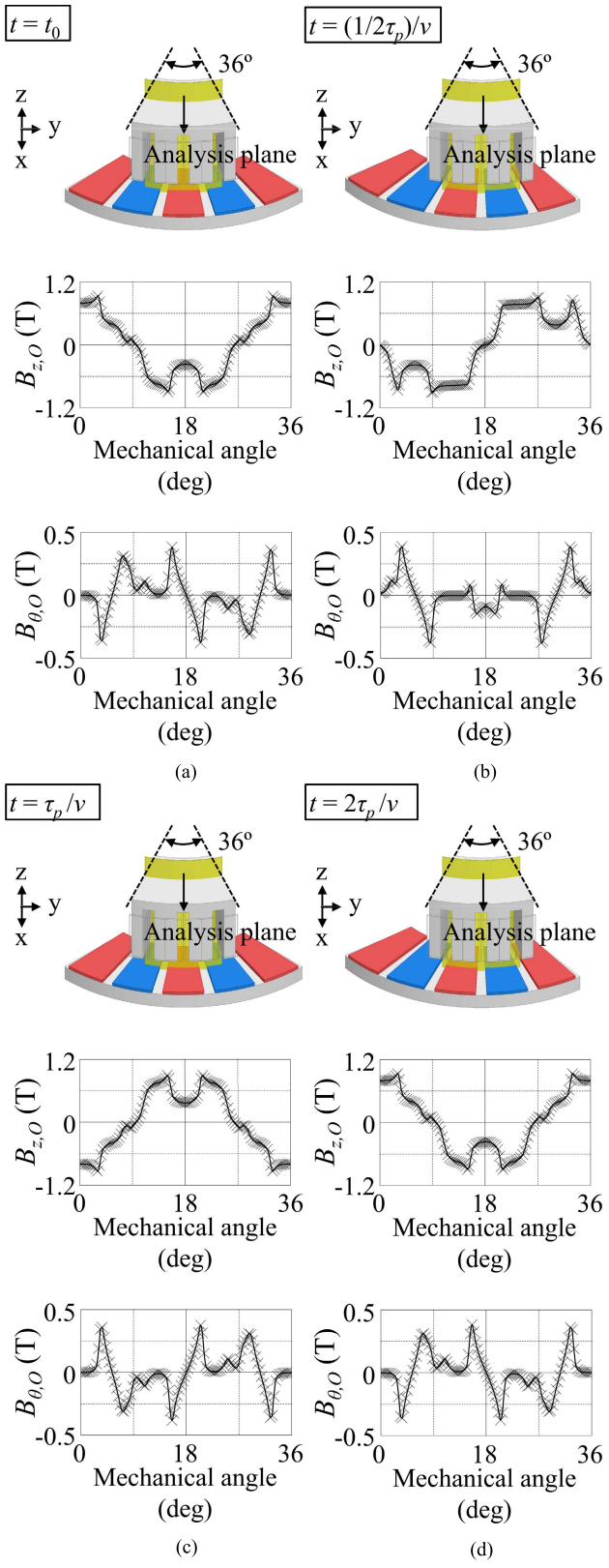

FIGURE 6. Open-circuit field. (a) Initial time. (b) Rotor moves by 1/2 pole pitch. (c) Rotor moves by pole pitch. (d) Rotor moves by 2 pole pitch.

Fig. 8 (a) and (b) describe the shape of the rotor when the skew angles are 0 and 6 degrees, respectively. The rotor

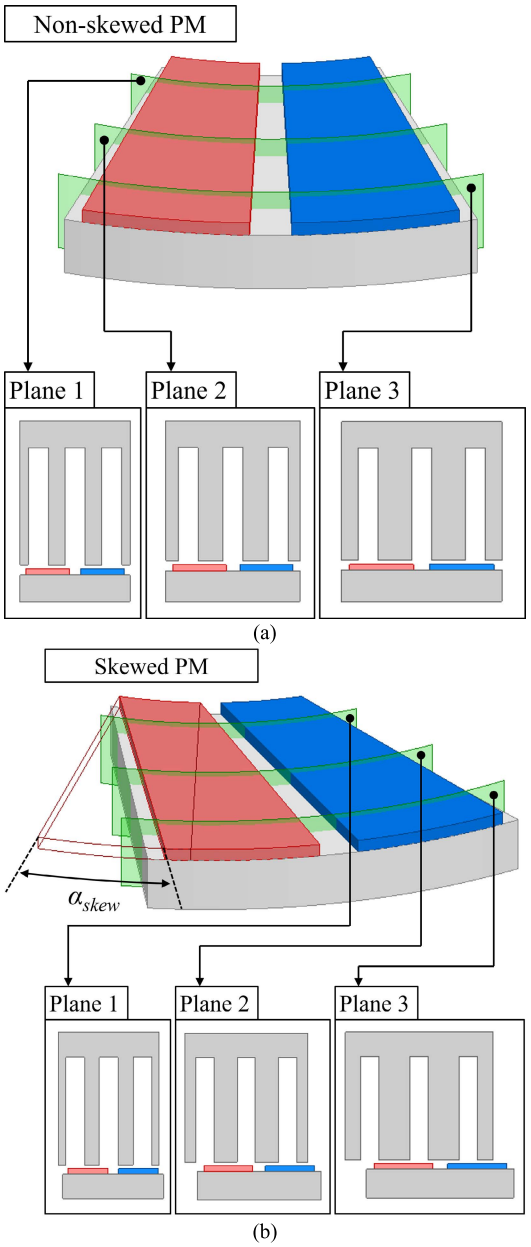

FIGURE 7. 2-D analysis plane. (a) Non-skewed PM. (b) Skewed PM.

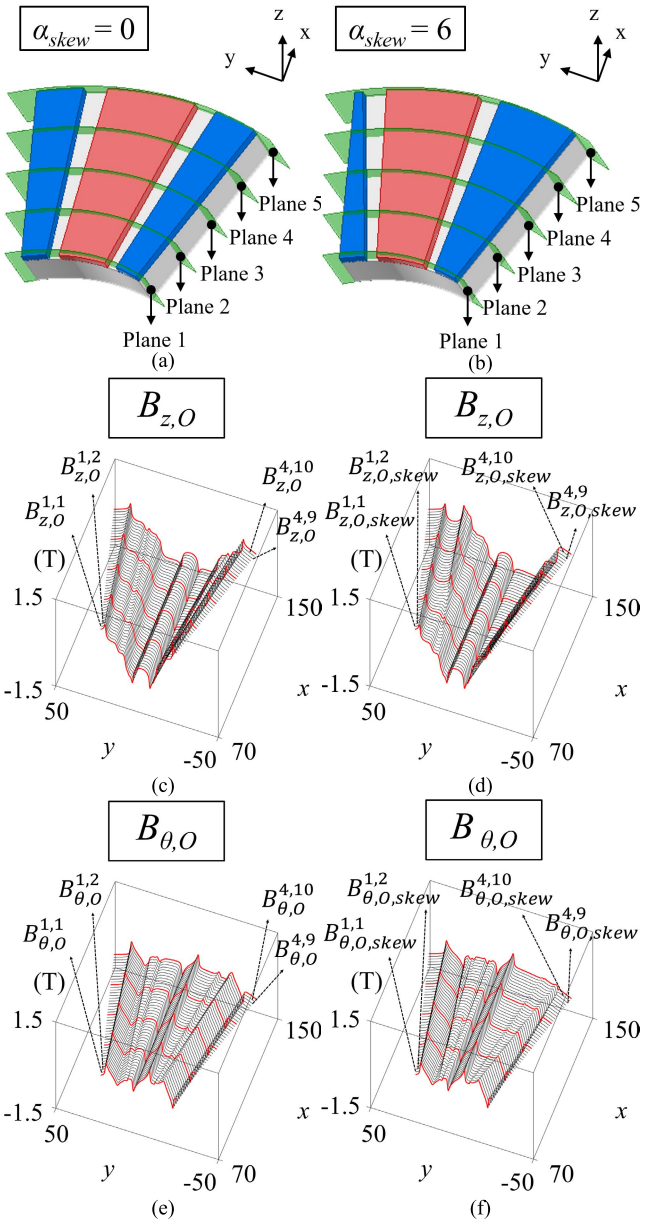

FIGURE 8. Air-gap flux distribution in the open-circuit field at the initial position. (a) 2-D analysis plane with non-skewed PM. (b) 2-D analysis plane with skewed PM. (c) z-component of open-circuit field with non-skewed PM. (d) z-component of open-circuit field with skewed PM. (e) θ-component of open-circuit field with non-skewed PM. (f) θ-component of open-circuit field with skewed PM.

is in its initial position and there are 5 2-D analysis planes. Each 2-D analysis plane has a radius in Table 1. Similar to the shape sweeping of the armature reaction field, the magnetic flux distributions on the 5 2-D analysis planes are first mapped to the problem domain. The spatial interpolation was performed with 10 lattices, and 10 virtual air-gap flux distributions were obtained in (11) using the basis function. Fig. 8 (c) and (e) show the z- and θ-components of the open-circuit field over a total of 45 air-gaps, respectively. Fig. 8 (d) and (f) are open-circuit fields when the skew angle is 6 degrees. These magnetic field distributions were reconstructed by the basis function in (12) using the magnetic field at the entire rotor position obtained through time sweeping in (10). As such, by using the basis function, it is possible to predict the change in magnetic flux distribution according to a specific PM skew angle without additional FE analysis, unlike the conventional quasi-3-D method.

IV. CHARACTERISTIC ANALYSIS

A. ELECTROMAGNETIC TORQUE

The electromagnetic torque in the proposed quasi-3-D analysis is calculated using Maxwell stress tensor (MST). The total air-gap magnetic flux density required for force calculation is obtained as

$$B_r(t, r, \theta, z) = B_{r,A}(t, r, \theta, z) + B_{r,O}(t, r, \theta, z) \quad (13)$$

TABLE 2. 2-D analysis plane for Characteristic analysis.

Number of 2-D analysis plane	6
Number of virtual air-gap section	55
Radius of Plane 1 (mm)	75
Radius of Plane 2 (mm)	88.5
Radius of Plane 3 (mm)	102
Radius of Plane 4 (mm)	115.5
Radius of Plane 5 (mm)	129
Radius of Plane 6 (mm)	142.5

$$B_\theta(t,r,\theta,z) = B_{\theta,A}(t,r,\theta,z) + B_{\theta,O}(t,r,\theta,z) \quad (14)$$

$$B_z(t,r,\theta,z) = B_{z,A}(t,r,\theta,z) + B_{z,O}(t,r,\theta,z) \quad (15)$$

where B_r, B_θ, and B_z are the r-direction, θ-direction, and z-direction components of the total air-gap magnetic flux density in the cylindrical coordinate system, respectively. Each total magnetic flux density is expressed as the sum of the armature reaction field and the open-circuit field reconstructed in (1) and (7).

Based on the MST, the force distribution in the cylindrical coordinate system is expressed as follows:

$$F = \int_S \overleftrightarrow{T} \cdot \hat{n}\, dS \quad (16)$$

$$\overleftrightarrow{T} = \begin{bmatrix} T_{rr} & T_{r\theta} & T_{rz} \\ T_{\theta r} & T_{\theta\theta} & T_{\theta z} \\ T_{zr} & T_{z\theta} & T_{zz} \end{bmatrix} = \begin{bmatrix} \frac{B_r^2 - B_\theta^2 - B_z^2}{2\mu_0} & \frac{B_r B_\theta}{\mu_0} & \frac{B_r B_z}{\mu_0} \\ \frac{B_r B_\theta}{\mu_0} & \frac{B_\theta^2 - B_r^2 - B_z^2}{2\mu_0} & \frac{B_\theta B_z}{\mu_0} \\ \frac{B_r B_z}{\mu_0} & \frac{B_\theta B_z}{\mu_0} & \frac{B_z^2 - B_r^2 - B_\theta^2}{2\mu_0} \end{bmatrix} \quad (17)$$

where F is the force distribution, S is the surface area in middle of the air-gap, $\hat{n}$ is the normal vector of S, $\overleftrightarrow{T}$ is the MST, and μ_0 is the vacuum permeability. The torque at each air-gap section is calculated as follows:

$$T_i = r_i \times \frac{1}{\mu_0} \iint_{\Delta S,i} (B_\theta B_z)\, d\theta dr \quad (18)$$

$$T = \sum_{i=1}^{N_{ag}} T_i \quad (19)$$

where T_i and r_i are the torque and radius of the i-th air-gap section, respectively, $\Delta S,i$ is the area of the i-th air-gap, N_{ag} is the total number of air-gaps, including the virtual air-gap obtained by the shape sweeping of the basis function and the air-gap on the 2-D analysis plane, and T is the total torque of the AFPMM.

The cogging torque under no-load condition can be calculated using the open-circuit field reconstructed in (7)-(10) as

$$T_{cogg.} = \sum_{i=1}^{N_{pl}} r_i \times \frac{1}{\mu_0} \iint_{\Delta S,i} \left(B_{\theta,O} B_{z,O}\right) d\theta dr. \quad (20)$$

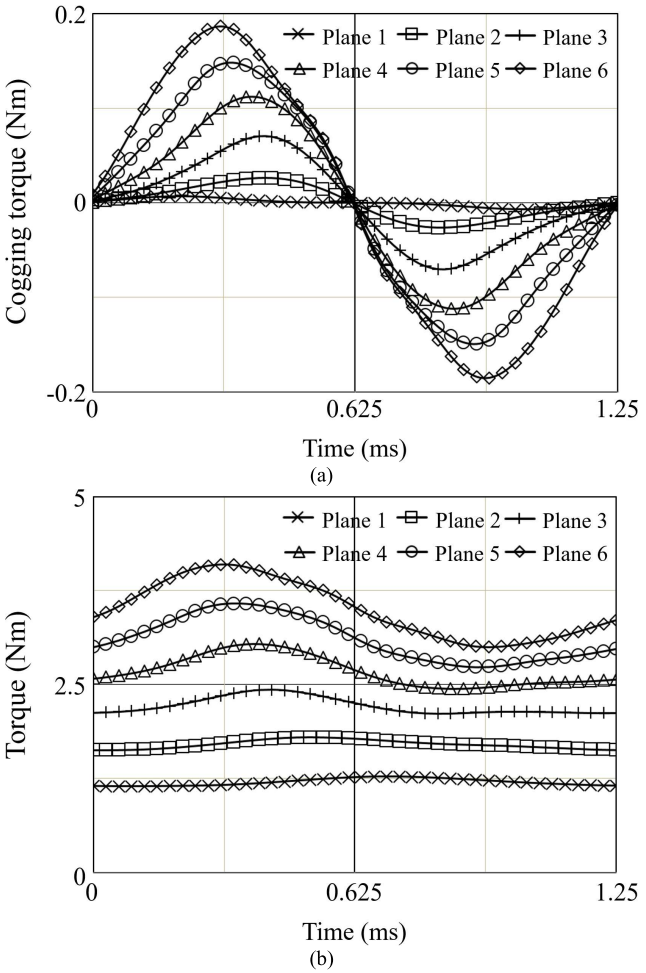

FIGURE 9. Electromagnetic torque for different 2-D analysis planes. (a) Cogging torque. (b) Load torque.

Fig. 9 (a) and (b) show the cogging torque and load torque corresponding to the 2-D analysis plane, respectively, and the radius of each 2-D analysis plane is given in Table 2. The electromagnetic torques in Fig. 9 only correspond to the 2-D analysis plane in (18), and the total torque in (19) is shown in Fig. 10. The magnetic flux distribution for torque calculation was obtained with 6 2-D analysis planes and 55 virtual air-gap sections. The virtual air-gap sections were obtained from the spatial field interpolated with 11 lattices. The cogging torque was calculated in (20) and the reconstructed open-circuit field in (7) was used. Using the reconstructed armature reaction field (1) and open-circuit field (7), the load torque was calculated in (18)-(19). In Fig. 9, it can be seen that the torque in each 2-D analysis plane increases as the radius increases, and the period is the same, but the shape of the waveform is not similar. This is because the ratio of slot opening to slot pitch is different and the magnetic flux density distribution over the air-gap is different.

Fig. 10 shows the cogging torque and load torque of the AFPMM with different PM skew angles. The PM skew angles are 0, 2, 4, and 6 degrees, respectively, and the analysis results for each model are compared in Table 3. For the

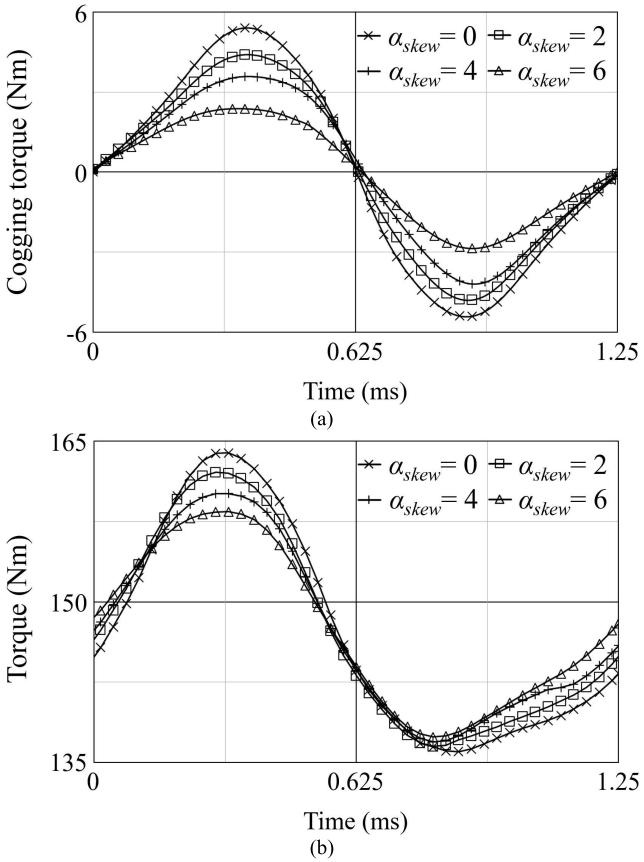

FIGURE 10. Electromagnetic torque for different PM skew angles (α_{skew}: 0, 2, 4, 6).

TABLE 3. Torque comparison.

PM skew angle (deg)	0	2	4	6
Cogging torque max. (Nm)	5.4	4.4	3.6	2.4
Reduction rate (%)	0	18.7	33.8	56.1
Load torque max. (Nm)	163.9	162.1	160.1	158.4
Reduction rate (%)	0	1.1	2.3	3.4
Load torque ripple (%)	18.9	17.3	15.7	14.2
Reduction rate (%)	0	8.4	17.0	24.8

calculation of the electromagnetic torque, the open-circuit field reconstructed by the shape sweeping of the basis function corresponding to each skew angle in (11), (12) was used. It is noted that the cogging torque is reduced due to PM skew, but the load torque is also reduced. Based on the non-skewed model, in the case of the model with a PM skew angle of 6 degrees, the load torque and load torque ripple decreased by 3.4% and 24.8%, respectively, when the cogging torque decreased by 56.1%.

B. ATTRACTION FORCE

Unlike the RFPMM, the AFPMM requires an auxiliary structure to maintain the air-gap, and accurate evaluation of the attraction force between the stator and rotor is essential. Using the tensor in (17), the attraction force can be calculated

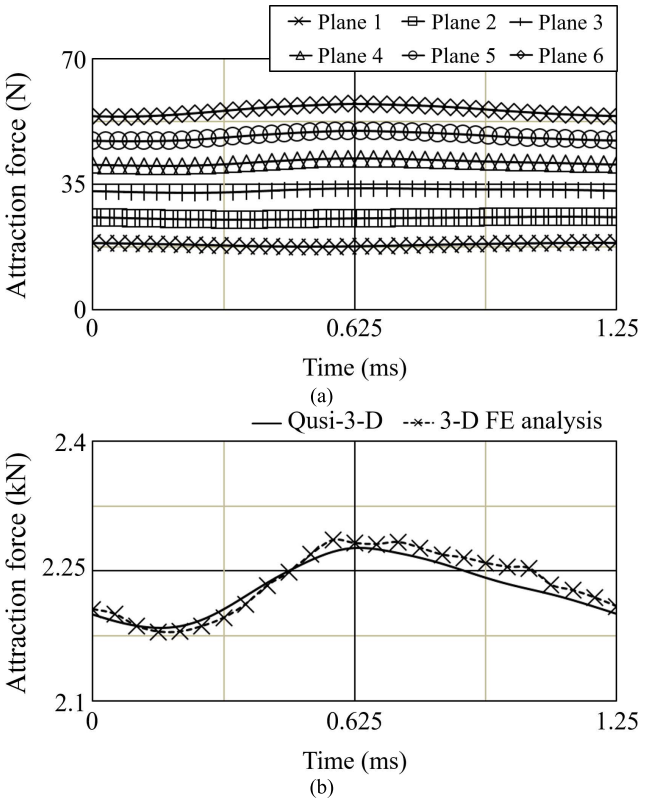

FIGURE 11. Attraction force. (a) Attraction force for different 2-D analysis planes. (b) Total attraction force.

as

$$F_{att.} = \sum_{i=1}^{N_{ag}} \frac{1}{2\mu_0} \iint_{\Delta S,i} \left(B_z^2 - B_r^2 - B_\theta^2 \right) d\theta dr. \quad (21)$$

where $F_{att.}$ is the total attraction force. when ignoring the radial magnetic flux density in the quasi-3-D analysis ($B_r = 0$), it can be simplified as follows:

$$F_{att.} = \sum_{i=1}^{N_{ag}} \frac{1}{2\mu_0} \iint_{\Delta S,i} \left(B_z^2 - B_\theta^2 \right) d\theta dr. \quad (22)$$

Fig. 11 (a) shows the attraction force according to different 2-D analysis planes calculated using (22). The total attraction force is compared with the 3-D FE analysis result in Fig. 11 (b). It is noted that the attraction force increases closer to the outer diameter, and the result of the total attraction force matches well with the 3-D FE analysis result with an error of less than 1.1%.

C. BACK-EMF

In AFPMM, most of the magnetic flux inside the stator passes through the tooth plane in Fig. 12. Assuming that the influence of the leakage flux is negligible, the flux linkage in the slot winding can be approximated as the magnetic flux through region Δz_a of the air-gap. Using the z-component of the magnetic flux distribution toward the tooth plane, the flux

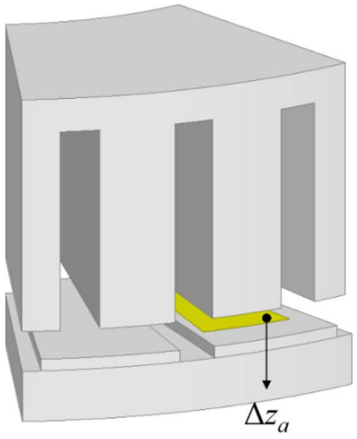

FIGURE 12. Tooth plane.

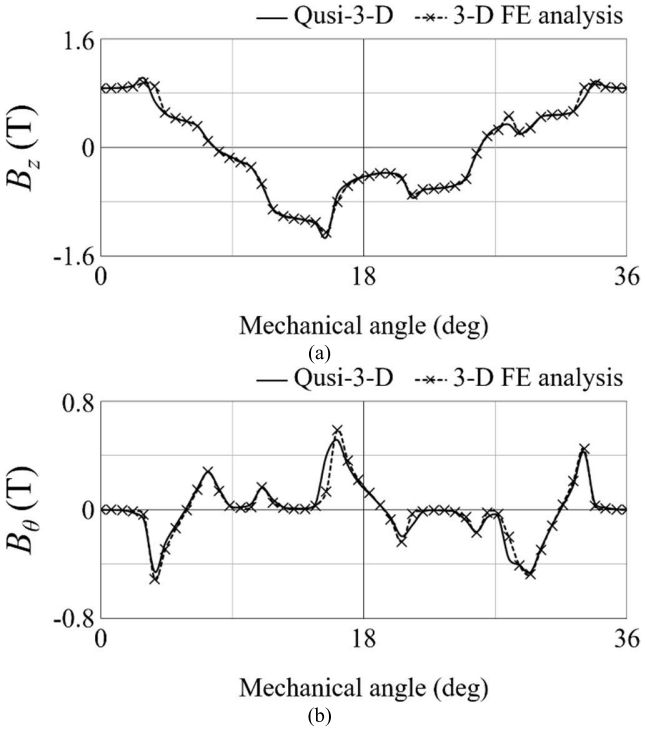

FIGURE 13. Total magnetic flux density in air-gap. (a) z-component. (b) θ-component.

linkage of each phase is calculated as follows:

$$\lambda_a(t) = N_a \cdot \iint_{\Delta z_a} \left(B_{z,A}(t) + B_{z,O}(t)\right) d\theta dr \tag{23}$$

where λ_a is the linkage flux in the a-phase winding, and N_a is the number of turns of a-phase winding. Based on the voltage equation and using the open-circuit field component of the flux linkage, the back-EMF is calculated as

$$\lambda_{a,noload}(t) = N_a \cdot \iint_{\Delta z_a} B_{z,O}(t)\, d\theta dr \tag{24}$$

$$e_a = \frac{d\lambda_{a,noload}}{dt} \tag{25}$$

where $\lambda_{a,noload}$ is the linkage flux in the a-phase winding under no load condition, and e_a is the a-phase back-EMF.

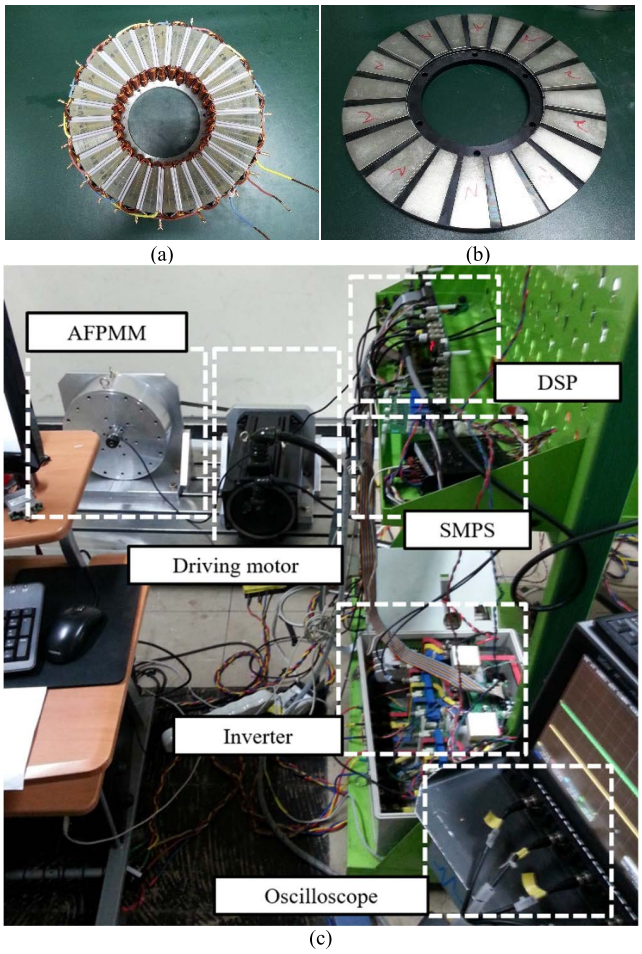

FIGURE 14. (a) Stator. (b) Rotor. (c) Test set.

V. RESULT

Fig. 13 shows the comparison of the air-gap flux densities in the proposed quasi-3-D FE analysis and the 3-D FE analysis. Fig. 13 (a) and (b) are the z-component and θ-component of the total magnetic flux density in (15) and (14), respectively. The magnetic flux distribution corresponds to the air-gap at the center radius of the AFPMM, 108.75mm, and the rotor is in the initial position. The difference between the proposed quasi-3-D FE analysis and 3-D FE analysis results is less than 1.7%.

Fig. 14 shows a prototype of the AFPMM for a 5 kW in-wheel motor. The specifications of design parameters are described in Table 4. The material for the stator and rotor back-irons is 35JN230. The material of PM is N42SH. The test set is shown in Fig. 14 (c). Fig. 15 shows the back EMF under no-load condition, for the non-skewed PM model and the model with the PM skew angle of 6 degrees, respectively. The proposed quasi-3-D analysis results were calculated in (25) using the open-circuit field in (7). Each analysis result has a mean error of 3.2% and 4.1%, respectively, compared to the measurement result.

In Fig. 16, the cogging torque for the model without PM skew and the model with a skew angle of 6 degrees is shown,

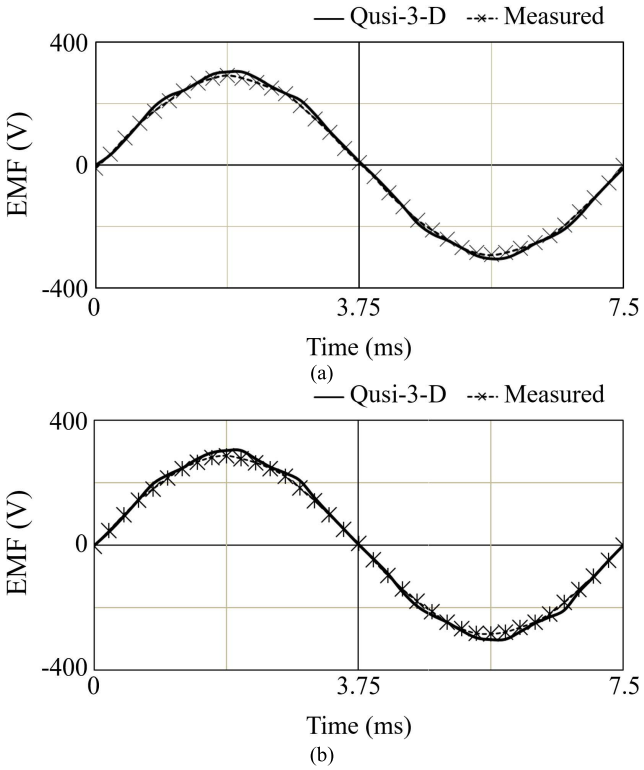

FIGURE 15. EMF. (a) AFPMM with non-skewed PM. (b) AFPMM with skewed PM.

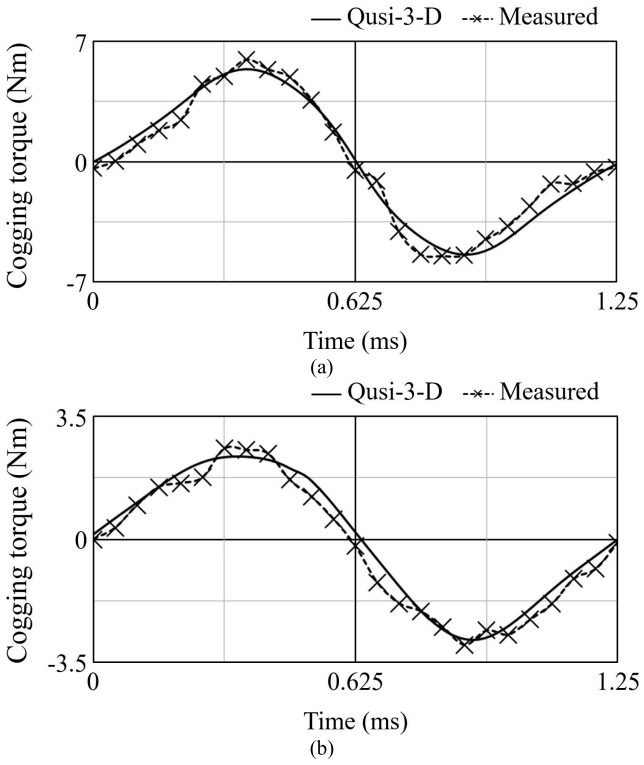

FIGURE 16. Cogging torque. (a) $\alpha_{skew} = 0$. (b) $\alpha_{skew} = 6$.

and the results of the proposed quasi-3-D analysis are compared with the experimental results. In the model with and without skew, the proposed quasi 3-D analysis results differed

TABLE 4. Specifications of Design Parameters for 5-kW In-Wheel Motor.

Number of poles	20
Number of slots (mm)	30
Inner diameter (mm)	150
Outer diameter (mm)	285
Air-gap (mm)	1.7
Motor length (mm)	88.5
Rated power (kW)	5
DC-link voltage (V_{dc})	300
Rated current (A_{peak})	28
Motor speed (rpm)	800

TABLE 5. Comparison with conventional quasi-3-D FE analysis.

	Conventional		Enhanced
Number of 2-D analysis plane	6	60	6
Load torque error (%)	8.42	2.31	2.31
Computational time reduction rate (%)	99.08	90.78	98.97

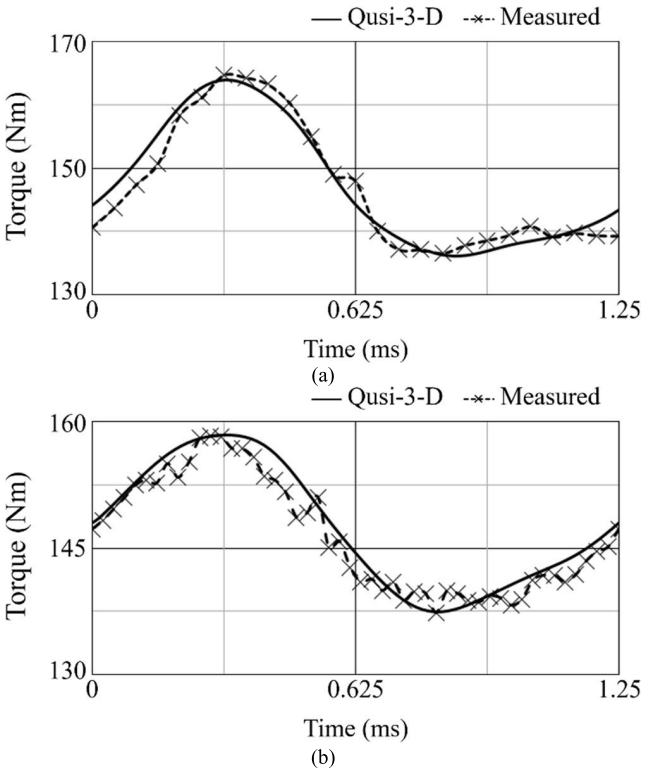

FIGURE 17. Load torque. (a) $\alpha_{skew} = 0$. (b) $\alpha_{skew} = 6$.

by 15.1% and 3.2%, respectively, compared to the measured results. In the case of the load torque, the results are compared in Fig. 17, and it can be seen that the errors of the results are acceptable as less than 1.7% and 2.3%, respectively.

Table 5 describes the comparison between the conventional quasi-3-D FE analysis and the proposed method. In the proposed quasi-3-D analysis, 6 2-D analysis planes were used. For the evaluation of the armature reaction field, the calculation time was reduced because the static FE analysis with 1 analysis step was performed using the time sweeping of the basis function, and the accuracy of the analysis result was increased because of the virtual air-gap section method

through the shape sweeping. Under the same simulation conditions (CPU Intel core i7-11700K, GPU RTX 3060 Ti, RAM 32GB, Elements 7344), to obtain the load torque result with an analysis error of less than 2.31%, the proposed method required 16 minutes and 16 seconds, whereas the conventional quasi 3-D method took 2 hours and 25 minutes. On the other hand, when using the same number of 2-D analysis planes as 6 in the conventional quasi-3-D method, an error of 8.42% occurs. Finally, the proposed quasi-3-D method provides a dramatic reduction of 98.97% compared to that the 3-D FE analysis took 27 hours and 2 minutes.

VI. CONCLUSION

This paper presented the characteristic analysis of AFPMM for 5-kW in-wheel motor using the novel quasi-3-D modeling. It has been investigated that the error in the conventional quasi-3-D FE analysis is caused by the change in the ratio of slot opening to slot pitch according to the radius. This makes a larger number of 2-D analysis planes required to ensure high accuracy of analysis results. In addition, in order to obtain accurate time-based analysis results, a large number of analysis time steps in transient FE analysis are required, which in turn increases the computational time burden. The method proposed in this paper reconstructs the air-gap magnetic flux distribution using a basis function. The magnetic field is reconstructed by sweeping the information of the magnetic flux distribution in a small number of 2-D analysis planes by the basis function, and two types of the sweeping are introduced: time sweeping and shape sweeping.

The time sweep of the basis function is based on the FR method, which allows the magnetic flux distribution for any rotor position and excitation current to be calculated without additional FE analysis. Since the static FE analysis with only one analysis step is performed to obtain the reference magnetic flux distribution, the computational burden is reduced compared to the transient FE analysis, which requires many analysis steps.

By using the basis function shape sweep, the magnetic flux distributions in the air-gap area except for the 2-D analysis plane are predicted. The magnetic flux distributions on the introduced virtual air-gap section between the 2-D analysis planes are calculated mathematically without additional FE analysis. In the spatial interpolation of the problem domain based on the Kriging method, a limited number of 2-D analysis planes were used as sampling data to calculate magnetic flux distributions in virtual air-gap sections. By using the virtual air-gap section, the analysis error of the quasi-3-D method is improved considering that the ratio of slot opening to slot pitch varies with radius.

In order to optimize the PM skew angle in the conventional quasi 3-D FE analysis, FE analysis should be performed whenever the skew angle is changed. On the other hand, the proposed technique can predict the air-gap flux distribution according to the changed PM skew angle using the reconstructed magnetic field. This simplifies the iteration of the optimization process, reducing the overall time cost and provides a reduction of 98.87% compared to 3-D FE analysis. This paper is expected to contribute to the effective analysis of the characteristics of AFPMMs used as in-wheel motors. The comparative study of several optimization techniques (e.g., overhang structures, new geometries of PM skew) is recommended as valuable future work.

REFERENCES

[1] D.-K. Lim, Y.-S. Cho, J.-S. Ro, S.-Y. Jung, and H.-K. Jung, "Optimal design of an axial flux permanent magnet synchronous motor for the electric bicycle," *IEEE Trans. Magn.*, vol. 52, no. 3, pp. 1–4, Mar. 2016.

[2] M. T. Girgin, M. K. Guven, and M. Aydin, "A new harmonic current injection technique to reduce cogging torque in axial flux permanent magnet motors," *IEEE Trans. Magn.*, vol. 58, no. 2, pp. 1–4, Feb. 2022.

[3] H.-J. Pyo, J. W. Jeong, J. Yu, S. G. Lee, and W.-H. Kim, "Design of 3D-printed hybrid axial-flux motor using 3D-printed SMC core," *IEEE Trans. Appl. Supercond.*, vol. 30, no. 4, pp. 1–4, Jun. 2020.

[4] K. Kim, B. Jeong, and D. Woo, "Optimal overhang structure considering overhang effects in the axial flux permanent magnet motor," *Int. J. Appl. Electromagn. Mech.*, vol. 58, no. 2, pp. 227–237, 2018.

[5] G. R. B. Bruzinga, A. J. S. Filho, and A. Pelizari, "Analysis and design of 3 kW axial flux permanent magnet synchronous motor for electric car," *IEEE Latin Amer. Trans.*, vol. 20, no. 5, pp. 855–863, May 2022.

[6] C. H. T. Lee, K. T. Chau, C. Liu, T. W. Ching, and F. Li, "A high-torque magnetless axial-flux doubly-salient machine for in-wheel direct drive applications," *IEEE Trans. Magn.*, vol. 50, no. 11, pp. 1–5, Nov. 2014.

[7] T. Takahashi, M. Takemoto, S. Ogasawara, W. Hino, and K. Takezaki, "Size and weight reduction of an in-wheel axial-gap motor using ferrite permanent magnets for electric commuter cars," *IEEE Trans. Ind. Appl.*, vol. 53, no. 4, pp. 3927–3935, Jul./Aug. 2017.

[8] D. Winterborne, N. Stannard, L. Sjåberg, and G. Atkinson, "An air-cooled YASA motor for in-wheel electric vehicle applications," *IEEE Trans. Ind. Appl.*, vol. 56, no. 6, pp. 6448–6455, Nov./Dec. 2020.

[9] M. Ehsani, K. V. Singh, H. O. Bansal, and R. T. Mehrjardi, "State of the art and trends in electric and hybrid electric vehicles," *Proc. IEEE*, vol. 109, no. 6, pp. 967–984, Jun. 2021.

[10] D. Shen, D. Karbowski, and A. Rousseau, "A minimum principle-based algorithm for energy-efficient eco-driving of electric vehicles in various traffic and road conditions," *IEEE Trans. Intell. Vehicles*, vol. 5, no. 4, pp. 725–737, Dec. 2020.

[11] B. S. Umesh, V. Khadkikar, H. H. Zeineldin, S. Singh, H. Otrok, and R. Mizouni, "Direct electric vehicle to vehicle (V2V) power transfer using on-board drivetrain and motor windings," *IEEE Trans. Ind. Electron.*, vol. 69, no. 11, pp. 10765–10775, Oct. 2021.

[12] M. L. De Klerk and A. K. Saha, "A comprehensive review of advanced traction motor control techniques suitable for electric vehicle applications," *IEEE Access*, vol. 9, pp. 125080–125108, 2021.

[13] S. A. Afsari, H. Heydari, and B. Dianati, "Cogging torque mitigation in axial flux magnetic gear system based on skew effects using an improved quasi 3-D analytical method," *IEEE Trans. Magn.*, vol. 51, no. 9, pp. 1–11, Sep. 2015.

[14] H. Tiegna, Y. Amara, and G. Barakat, "A new quasi-3-D analytical model of axial flux permanent magnet machines," *IEEE Trans. Magn.*, vol. 50, no. 2, pp. 817–820, Feb. 2014.

[15] A. A. Arkadan, T. M. Hijazi, and B. Masri, "Design evaluation of conventional and toothless stator wind power axial-flux PM generator," *IEEE Trans. Magn.*, vol. 53, no. 6, pp. 1–4, Jun. 2017.

[16] J. Wanjiku, M. A. Khan, P. S. Barendse, and P. Pillay, "Influence of slot openings and tooth profile on cogging torque in axial-flux PM machines," *IEEE Trans. Ind. Electron.*, vol. 62, no. 12, pp. 7578–7589, Dec. 2015.

[17] A. Hemeida, A. Lehikoinen, P. Rasilo, H. Vansompel, A. Belahcen, A. Arkkio, and P. Sergeant, "A simple and efficient quasi-3D magnetic equivalent circuit for surface axial flux permanent magnet synchronous machines," *IEEE Trans. Ind. Electron.*, vol. 66, no. 11, pp. 8318–8333, Nov. 2019.

[18] J. Azzouzi, G. Barakat, and B. Dakyo, "Quasi-3-D analytical modeling of the magnetic field of an axial flux permanent-magnet synchronous machine," *IEEE Trans. Energy Convers.*, vol. 20, no. 4, pp. 746–752, Dec. 2005.

[19] A. Parviainen, M. Niemela, and J. Pyrhonen, "Modeling of axial permanent-magnet machines," *IEEE Trans. Ind. Appl.*, vol. 40, no. 5, pp. 1333–1340, Sep. 2004.
[20] K. H. Kim and D. K. Woo, "Field reconstruction method for linear tubular permanent magnet motor," *IEEE Access*, vol. 8, pp. 169516–169524, 2020.
[21] H. J. Park, H. K. Jung, S. Y. Jung, Y. H. Chae, and D. K. Woo, "Field reconstruction method in axial flux permanent magnet motor with overhang structure," *IEEE Trans. Magn.*, vol. 53, no. 6, pp. 1–4, Jun. 2017.
[22] E. Ajily, K. Abbaszadeh, and M. Ardebili, "Three-dimensional field reconstruction method for modeling axial flux permanent magnet machines," *IEEE Trans. Energy Convers.*, vol. 30, no. 1, pp. 199–207, Mar. 2015.
[23] K. H. Kim, H. K. Cho, and D. K. Woo, "3D characteristic analysis of 3-leg linear permanent magnet motor with magnet skew and overhang structure," *IEEE Access*, vol. 9, pp. 153863–153874, 2021.
[24] D.-K. Woo, I.-W. Kim, D.-K. Lim, J.-S. Ro, and H.-K. Jung, "Cogging torque optimization of axial flux permanent magnet motor," *IEEE Trans. Magn.*, vol. 49, no. 5, pp. 2189–2192, May 2013.
[25] S. Bhattacharjee and S. K. Ghosh, "Performance evaluation of semantic Kriging: A Euclidean vector analysis approach," *IEEE Geosci. Remote Sens. Lett.*, vol. 12, no. 6, pp. 1185–1189, Jun. 2015.
[26] P.-W. Son, J. H. Rhee, J. Hwang, and J. Seo, "Universal Kriging for Loran ASF map generation," *IEEE Trans. Aerosp. Electron. Syst.*, vol. 55, no. 4, pp. 1828–1842, Aug. 2019.
[27] A. Pietrenko-Dabrowska, S. Koziel, and M. Al-Hasan, "Cost-efficient bi-layer modeling of antenna input characteristics using gradient Kriging surrogates," *IEEE Access*, vol. 8, pp. 140831–140839, 2020.
[28] A. Pietrenko-Dabrowska and S. Koziel, "Antenna modeling using variable-fidelity EM simulations and constrained co-Kriging," *IEEE Access*, vol. 8, pp. 91048–91056, 2020.
[29] M. E. Diago-Mosquera, A. Aragon-Zavala, F. A. Rodriguez-Corbo, M. Celaya-Echarri, R. Shubair, and L. Azpilicueta, "Tuning selection impact on Kriging-aided in-building path loss modeling," *IEEE Antennas Wireless Propag. Lett.*, vol. 21, no. 1, pp. 84–88, Jan. 2022.
[30] K. Wang and H. Lin, "A novel 24-slot/10-pole dual three-phase fractional-slot overlapped winding for low non-working space harmonics and stator modularization," *IEEE Access*, vol. 8, pp. 85490–85503, 2020.
[31] J. A. Güemes, A. M. Iraolagoitia, J. I. Del Hoyo, and P. Fernández, "Torque analysis in permanent-magnet synchronous motors: A comparative study," *IEEE Trans. Energy Convers.*, vol. 26, no. 1, pp. 55–63, Mar. 2011.
[32] S.-K. Lee, G.-H. Kang, J. Hur, and B.-W. Kim, "Quasi-zero torque pulsation of surface permanent magnet synchronous motor for ship gyro stabilizer by pole/slot number and air-gap designs," *IEEE Trans. Magn.*, vol. 50, no. 2, pp. 797–800, Feb. 2014.
[33] V. Simón-Sempere, A. Simón-Gómez, M. Burgos, and J.-R. Cerquides-Bueno, "Optimisation of magnet shape for cogging torque reduction in axial-flux permanent-magnet motors," *IEEE Trans. Energy Convers.*, vol. 36, no. 4, pp. 2825–2838, Dec. 2021.
[34] B. Dai, K. Nakamura, Y. Suzuki, Y. Tachiya, and K. Kuritani, "Cogging torque reduction of integer gear ratio axial-flux magnetic gear for wind-power generation application by using two new types of pole-pieces," *IEEE Trans. Magn.*, vol. 58, no. 8, pp. 1–5, Aug. 2022.
[35] S. Leitner, H. Gruebler, and A. Muetze, "Cogging torque minimization and performance of the sub-fractional HP BLDC claw-pole motor," *IEEE Trans. Ind. Appl.*, vol. 55, no. 5, pp. 4653–4664, Sep./Oct. 2019.
[36] S. Leitner, G. Krenn, H. Gruebler, and A. Muetze, "Rheometer-based cogging and hysteresis torque and iron loss determination of sub-fractional horsepower motors," *IEEE Trans. Ind. Appl.*, vol. 56, no. 4, pp. 3679–3690, Jul./Aug. 2020.
[37] S. W. Lee, I. J. Yang, and W. H. Kim, "A study on reducing cogging torque of IPMSM applying rotating tapering," *IEEE Trans. Magn.*, vol. 58, no. 8, pp. 1–5, Aug. 2022.
[38] I.-H. Jo, H.-W. Lee, G. Jeong, W.-Y. Ji, and C.-B. Park, "A study on the reduction of cogging torque for the skew of a magnetic geared synchronous motor," *IEEE Trans. Magn.*, vol. 55, no. 2, pp. 1–5, Feb. 2019.
[39] H. Jang, H. Kim, D.-W. Nam, W.-H. Kim, J. Lee, and C. Jin, "Investigation and analysis of novel skewing in a 140 kW traction motor of railway cars that accommodate limited inverter switching frequency and totally enclosed cooling system," *IEEE Access*, vol. 9, pp. 121405–121413, 2021.
[40] O. Ocak and M. Aydin, "An innovative semi-FEA based, variable magnet-step-skew to minimize cogging torque and torque pulsations in permanent magnet synchronous motors," *IEEE Access*, vol. 8, pp. 210775–210783, 2020.
[41] D. Barman and P. Pillay, "Effect of skewing in a variable flux interior permanent magnet synchronous machine," *IEEE Trans. Ind. Appl.*, vol. 56, no. 6, pp. 6399–6410, Nov./Dec. 2020.
[42] M. Aydin and M. Gulec, "Reduction of cogging torque in double-rotor axial-flux permanent-magnet disk motors: A review of cost-effective magnet-skewing techniques with experimental verification," *IEEE Trans. Ind. Electron.*, vol. 61, no. 9, pp. 5025–5034, Sep. 2014.
[43] A. Mahmoudi, S. Kahourzade, N. A. Rahim, and W. P. Hew, "Design, analysis, and prototyping of an axial-flux permanent magnet motor based on genetic algorithm and finite-element analysis," *IEEE Trans. Magn.*, vol. 49, no. 4, pp. 1479–1492, Apr. 2013.
[44] D.-K. Woo, J.-H. Choi, M. Ali, and H.-K. Jung, "A novel multimodal optimization algorithm applied to electromagnetic optimization," *IEEE Trans. Magn.*, vol. 47, no. 6, pp. 1667–1673, Jan. 2011.
[45] T. D. Nguyen, K.-J. Tseng, S. Zhang, and H. T. Nguyen, "A novel axial flux permanent-magnet machine for flywheel energy storage system: Design and analysis," *IEEE Trans. Ind. Electron.*, vol. 58, no. 9, pp. 3784–3794, Sep. 2011.
[46] M. Polat, A. Yildiz, and R. Akinci, "Performance analysis and reduction of torque ripple of axial flux permanent magnet synchronous motor manufactured for electric vehicles," *IEEE Trans. Magn.*, vol. 57, no. 7, pp. 1–9, Jul. 2021.

KI-HOON KIM received the B.S. degree in electrical engineering from Yeungnam University, Gyengbuk, South Korea, in 2017, where he is currently pursuing the Ph.D. degree in electrical engineering.

His current research interests include numerical analysis and design of electrical machines.

DONG-KYUN WOO received the B.S. degree in electrical engineering from Yonsei University, Seoul, South Korea, in 2007, and the Ph.D. degree from Seoul National University, Seoul, in 2014.

He conducted research at the Power and Industrial Systems Research and Development Center of Hyosung, from 2014 to 2015. He is currently a Professor with the School of Electrical Engineering, Yeungnam University, Gyengbuk, South Korea. His research interests include numerical analysis and design of the electric machines.